TECHNICAL PAPER

A longitudinal study of a lateral intracranial aneurysm: identifying the hemodynamic parameters behind its inception and growth using computational fluid dynamics

I. L. Oliveira[1] · G. B. Santos[1] · J. Militzer[2] · C. E. Baccin[3] · R. T. Tatit[4] · J. L. Gasche[1]

Abstract

In the last two decades, the application of computational fluid dynamics (CFD) to study the blood flow in intracranial aneurysms has gained popularity since hemodynamics plays a key role in the inception, growth, and rupture of these aneurysms. Although the rupture event has been the main focus of these studies, other researches have shown the importance of hemodynamics also on the initiation and growth of intracranial aneurysms. However, due to the lack of follow up examinations of a single aneurysm case, these studies are scarcer. In this work, two consecutive examinations of an unruptured lateral aneurysm followed up for 5 years were used to investigate the growth of the aneurysm by using CFD. By simulating the flow in these two geometries and in the virtually reconstructed hypothetical healthy vasculature, correlations between hemodynamic parameters and the growth of the aneurysm were evaluated. The results showed that the inception of the aneurysm correlated positively with high wall shear stress (WSS) and high positive WSS spatial gradient, as other studies also suggest. Furthermore, and most importantly, as different biological pathways may explain the influence of hemodynamics on the growth process, the results also pointed out that the hemodynamic effects that drove the subsequent growth of the aneurysm have changed to a combination of low WSS and high oscillatory shear index (OSI). Thus, even though the driving mechanisms observed during each period are distinct, they strongly agree with two main theories that currently explain aneurysm inception and growth.

Keywords Computational fluid dynamics · Intracranial aneurysms · Aneurysm growth · Hemodynamics

1 Introduction

Intracranial aneurysms (IAs) are pathological dilatations in the vascular system occurring in the arteries that reach the brain. They are usually found in bifurcations of the vessel

tree (terminal aneurysms) or laterally to the arteries (lateral aneurysms, Fig. 1). Most of them are asymptomatic and represent a high risk to the patient if they rupture, being the subarachnoid hemorrhage (SAH) one of the most dangerous and common outcomes. In a review by Nieuwkamp et al. [1], the authors found that aneurysmal SAH case fatality varies from 27 to 44% and, among the studies that the authors selected in their review that reported SAH outcome, 19% of the patients present morbidity, a high fatality rate especially when reports show that SAH is caused by aneurysm rupture in 85% of cases [2].

Although in very early studies aneurysms were considered a congenital disease [3], it is widely accepted today that they are acquired lesions related to the interaction between the hemodynamic environment in the aneurysm lumen and its wall. In this context, the wall shear stress (WSS) is one of the most important factors because it acts as a mechanical regulator to several processes occurring in the vessel tissue—in the studies cited in this section, WSS generally means the *time-averaged* WSS magnitude over one cardiac

✉ J. L. Gasche
jose.gasche@unesp.br

1 Mechanical Engineering Department, São Paulo State University (UNESP) School of Engineering, Thermal Sciences Building, Avenida Brasil, 56, Ilha Solteira, SP, Brazil

2 Department of Mechanical Engineering, Dalhousie University, Halifax, Canada

3 Interventional Neuroradiology, Hospital Israelita Albert Einstein, São Paulo, Brazil

4 Albert Einstein Israeli Faculty of Health Sciences, São Paulo, Brazil
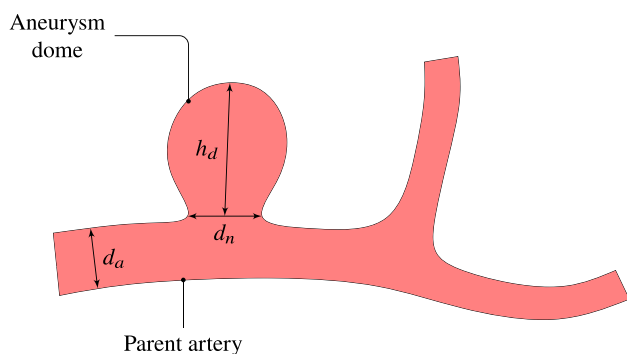
Fig. 1 Schematic of a typical lateral IA occurring in the internal carotid artery (ICA), indicating the main one-dimensional sizes: aneurysm dome height, h_d; aneurysm neck diameter, d_n; and the parent artery diameter, d_a

cycle since the WSS is a vector, whose precise definition is postponed to the methodology section. Biological changes in the arterial wall have already been shown to be related to abnormal levels of WSS on the vessel wall lumen: from changes in its permeability [4] to a possible indicator of atherosclerosis [5] and plaque formation, which has been correlated with low and oscillating shear stress since early studies [6]. Furthermore, the changes in WSS caused by abnormal hemodynamics are rapidly sensed by the endothelial cells lining the vascular lumen, triggering biological signals that not only regulate vascular tone but also initiate vascular remodeling when WSS deviates from baseline values [7]. For example, after surgically creating a bifurcation in a dog's artery, Meng et al. [8] mapped high levels of WSS and high positive WSS spatial gradient on the flanks of the bifurcation with destructive remodeling of the artery, characterized by internal elastic lamina disruption, endothelial cells loss with smooth muscle cells reduction and media thinning that resembles the type of vascular remodeling found in aneurysm samples [9]. Other studies supported their findings [10] and, currently, most studies agree that the inception of IAs occurs due to abnormally high WSS together with positive WSS spatial gradients [11], normally called "high-flow" effects acting on the vessels surface.

While Meng et al. [8] focused on bifurcation aneurysms, it is generally accepted that lateral aneurysms also initiate in regions of high-flow effects [12]. Lauric et al. [13] explored the influence of the ICA inner bend curvature on the onset of lateral aneurysms by virtually reconstructing the hypothetical healthy parent artery. In contrast with healthy arteries with similar morphological features, their conclusions suggest that peak local curvature in the arteries that developed aneurysms correlates with regions of high WSS, flanked by high and positive WSS spatial gradient.

Other studies proposed new hemodynamic parameters that may indicate the initiation site of an aneurysm [14, 15].

Mantha et al. [14] virtually reconstructed the healthy artery to study the initiation of three paraclinoid lateral aneurysms through a "potential" aneurysm formation indicator (AFI) that measures the degree of misalignment of the instantaneous WSS vector with its time-averaged direction. They based this definition on the biological observation that healthy endothelial cells are oriented according to the time-averaged WSS vector direction. Thus, randomly oriented vectors during the cardiac cycle could "trigger pathological changes in the endothelial cells, leading to aneurysm formation." Their results suggest that aneurysm formation occurs in regions of low AFI—i.e. AFI ≈ -1.0.

However, the physical mechanism responsible for the growth of an IA is still not well understood. The literature suggests both low-flow and high-flow effects as driving mechanisms for the evolution of an IA [11]. In general, low-flow effects are a synonym to lower WSS values with high oscillatory shear index (OSI) on the aneurysm surface—OSI is a measure of the temporal fluctuations in the direction of the WSS vector over the cardiac cycle [16]. Low-flow effects are responsible for blood flow stagnation adjacent to the vessel lumen, which causes accumulation of blood cells—red blood cells, leukocytes, and platelets [17]. Inflammatory cells cause degradative processes on the wall, which are exacerbated by the formation of plaque caused by low and oscillating WSS, as highlighted by Meng et al. [11], driving aneurysm growth. High-flow effects, on the other hand, are a synonym of high WSS with high positive WSS spatial gradients, that is, the same mechanisms responsible for the aneurysm inception. Of course, due to the complex flow that may emerge inside an aneurysm lumen depending on its morphology, both effects can occur on the aneurysm surface. Meng et al. [11] also related these two pathways with different morphological features that may arise in the aneurysm wall.

In this context, computational fluid dynamics (CFD) has been widely used to simulate the flow in virtual and patient-specific aneurysms geometries and vessel networks. The simulations have been used to improve the understanding of the flow dynamics and to correlate morphological and hemodynamic discriminants with aneurysm rupture [18–22]. While several CFD studies have been performed using aneurysm geometries obtained at a single instant of time, few studies have considered the time evolution of IAs [23, 24]. However, they studied only a single geometry over the temporal evolution of the aneurysm.

To the authors' knowledge, CFD studies concerning aneurysm inception and growth performed with two patient-specific aneurysm images obtained over time have not been reported. The objective of this work is to investigate the correlation between hemodynamic parameters and the growth of a lateral IA following its evolution during 5 years. The inception of the aneurysm was also studied

by virtually reconstructing the hypothetical healthy parent artery, which allowed the evaluation of two periods of the aneurysm evolution.

2 Methodology

2.1 Images and geometry segmentation

The case studied is a saccular lateral aneurysm born in the ophthalmic segment of the ICA, a common location of this kind of aneurysm. Two successive geometries obtained from digital subtraction angiography (DSA) examinations collected retrospectively were used to follow the evolution of the aneurysm.

The geometries of the vessel network and the aneurysm were segmented using the Vascular Modeling Toolkit (VMTK)®library with the level-sets segmentation approach [25]. Figure 2b and c shows the aneurysm geometry on the ICA inner bend at two different stages, labeled T1 and T2, when the aneurysm height was 1.6 mm and 4 mm, respectively. A large portion of the ICA and the daughter arteries—the anterior cerebral artery (ACA), the middle cerebral artery (MCA), and the ophthalmic artery (OA)—were included to avoid the influence of the inlet and outlets positions on the intra-aneurysmal and peri-aneurysmal flow [26]. At these positions, the diameter of each artery was: 3.8 mm at the ICA inlet, 2.4 mm, 1.8 mm, and 0.9 mm at the MCA, ACA, and OA outlets, respectively.

The hypothetical healthy artery was reconstructed by virtually removing the aneurysm at stage T1 by applying a local Laplacian filter on the aneurysm portion, i.e., the aneurysm surface was consecutively smoothed until only the parent artery remained. The final reconstructed healthy vasculature was labeled T0 (Fig. 2a). Although this procedure is operator dependent, it preserves the surrounding vasculature. Nevertheless, it is reasonable to expect that the overall vascular geometry would remain the same between stages T0 and T1 because they are almost identical when the vascular geometries of stages T1 and T2 are compared—except for possible minor differences arising from the segmentation process.

2.2 Physical and mathematical model of the blood flow

The governing equations for an incompressible, isothermal, and laminar flow, written in the integral form for a control volume V, with surface S, are:

$$\oint_S \rho v \cdot n \, dS = 0, \tag{1}$$

and

$$\frac{\partial}{\partial t} \int_V \rho v(x,t) dV + \oint_S \rho v v \cdot n \, dS$$
$$= -\oint_S p n \, dS + \oint_S \tau \cdot n \, dS, \tag{2}$$

where $\rho = 1056 \, \text{kg/m}^3$ is the blood density [27], n is the normal unit vector to S pointing outwards, v is the flow velocity field, p is the hydrostatic pressure, and τ is the viscous part of the Cauchy stress tensor, which for a Newtonian fluid is given by:

$$\tau = \mu^f \left(\nabla v + \nabla^T v \right), \tag{3}$$

where $\mu^f = 3.5 \times 10^{-3} \, \text{Pa s}$ is the dynamic viscosity of the blood [27, 28]. Equation (3) can be directly substituted into Eq. (2) to yield the Navier–Stokes equations. The Newtonian model was chosen after verifying that in the aneurysm sacs and surrounding arteries strain rates were much higher than $100 \, \text{s}^{-1}$, a well-known level below which the non-Newtonian behavior of blood is revealed [29].

A trivial initial condition was used for the velocity and pressure fields, i.e., they were assumed zero throughout the domain. At the inlet, a time-varying blood flow rate, $\bar{q}_a(t)$, corresponding to the flow pulse from the beginning of systole until the end of the diastole (Fig. 3) was imposed. This
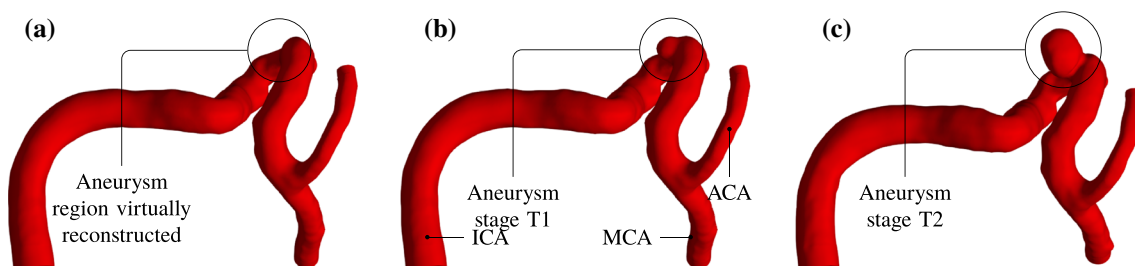
Fig. 2 **a** Vessel network virtually reconstructed and labeled as stage T0; **b** vessel network and aneurysm geometry at the stage T1, and **c** vessel network and aneurysm geometry at the stage T2
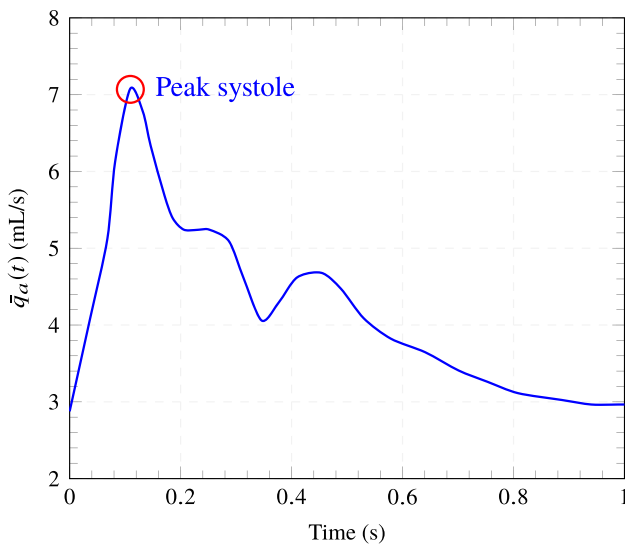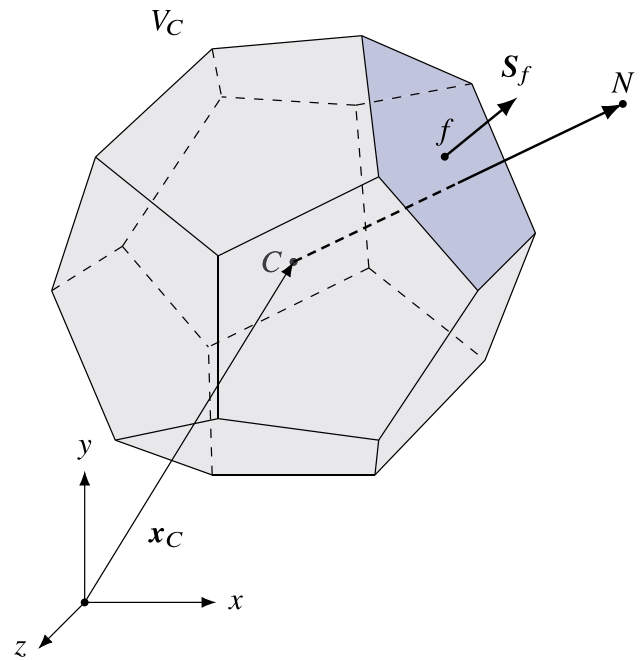
Fig. 3 Instantaneous flow rate profile in the internal carotid artery (prepared by the authors with data from Ford et al. [30] and Zarrinkoob et al. [31])

Fig. 4 Polyhedral control volume V_C with its geometric parameters used in the finite-volume discretization; N is the centroid of a neighboring cell

flow rate was obtained by multiplying the normalized flow rate reported by Ford et al. [30] by the mean blood flow rate in the aneurysm parent artery (ICA), $\bar{q}_a = 4.3$ ml/s, reported by Zarrinkoob et al. [31]. This average flow rate was used because the patient-specific blood flow rate waveform at the ICA was not available. The parabolic velocity profile for a fully developed laminar flow in a pipe was used for the spatial velocity distribution at the inlet,

$$v_{\text{inlet}}(r) = 2\frac{\bar{q}_a}{A_{\text{inlet}}}\left[1 - \frac{4r^2}{d_a^2}\right],$$ (4)

where A_{inlet} is the cross-sectional area of the inlet artery, d_a is its diameter, and r is the radial coordinate of the circular inlet section—an artificial circular section extension was added to the artery inlet to impose this inlet flow condition. Additionally, the pressure gradient was set to zero at the inlet.

To obtain the correct pressure in the results, a flux-corrected velocity with a constant pressure equal to 100 mmHg (13, 333 Pa)—the averaged human body pressure level for a cardiac cycle—was prescribed as boundary conditions at the outlet sections. Since the distances between the outlets and the aneurysm are sufficiently large, this boundary condition approximates the outflow resistance condition [26], in which the outlet pressure is proportional to the flow rate. The vessel walls were considered rigid with zero mass flux, zero pressure gradient, and no-slip as boundary conditions. Although there is evidence suggesting that the elasticity of the wall may impact the hemodynamic results [32, 33], the eventual changes in hemodynamics caused by the wall elasticity

would be consistent among the three geometries simulated, since our comparison was based on a single vasculature case. Then, it is reasonable to consider that the conclusions drawn from our analysis would not be invalidated by using the rigid wall model.

2.3 Numerical methodology

2.3.1 Equations discretization

The mathematical model was solved using the `foam-extend-4.0` CFD package [34, 35], which implements the Finite Volume Method (FVM) to discretize the governing equations, yielding a second-order accurate discretization, with collocated variables arranged in a cell-centered manner. A finite-volume mesh used by `foam-extend` is composed of non-overlapping polyhedral cells with polygonal flat faces (Fig. 4).

The first step in this particular implementation of the FVM is to write the governing equations, Eqs. (1)–(3), for the polyhedral cell shown in Fig. 4. By using the second-order Euler scheme to discretize the temporal term, we find the following semi-discretized equations:

$$\sum_f \dot{m}_f = 0,$$ (5)

$$\rho_C \frac{3 V_C^n \boldsymbol{v}_C^n - 4 V_C^{n-1} (\boldsymbol{v}_C)^{n-1} + V_C^{n-2} (\boldsymbol{v}_C)^{n-2}}{2\Delta t}$$
$$+ \sum_f \dot{m}_f \boldsymbol{v}_f^n = \sum_f \mu_f^{\mathrm{f}} (\nabla \boldsymbol{v})_f^n \cdot \boldsymbol{S}_f^{\,n} + (\nabla p)_C^n V_C^{\,n}, \qquad (6)$$

where the subscripts f and C represent values evaluated at the control volume face and centroid, respectively. The superscript "n" represents the current time level, $\dot{m}_f = \rho \boldsymbol{v}_f \cdot \boldsymbol{S}_f$ is the mass flow rate through face f, which must satisfy the mass conservation principle, Eq. (5), where $\boldsymbol{S}_f$ is the normal vector to face f pointing outward. The flow rate $\dot{m}_f$ is evaluated explicitly, i.e. from values available from the last iteration to linearize the advective term.

To complete the discretization procedure, the face values are interpolated using the cell centroid values and, to assure the second-order accuracy level, only second-order interpolation profiles were selected: the second-order upwind scheme for the advective term discretization with the Green-Gauss scheme for both velocity and pressure gradients discretizations and the second-order central differences for the surface-normal gradient in the diffusion term with non-orthogonal and skew corrections [36, 37]. The pressure implicit with splitting operators (PISO) algorithm [38] was used as the pressure-velocity coupling algorithm. Therefore, a pressure equation is derived from Eq. (5). Once discretized for a cell, the resulting algebraic linearized equations are assembled in two systems of equations for the velocity and pressure fields.

Finally, the solution algorithm is as follows:

(1) solve the discretized momentum equation for flow velocity components sequentially and separately, with the available pressure and velocity fields (in the first time-step, use initial condition values; after the first time-step, use values of the last coupling iteration); then start the PISO loop;
(2) with the momentum-satisfying velocity field, solve the pressure system of equations;
(3) correct the flow velocity field with the new continuity-satisfying pressure and mass flow rate fields and iterate over the pressure equation;
(4) calculate the residuals and check for convergence, if not converged, return to step 2.

Normalized residuals of 1×10^{-6} for the pressure equation and 1×10^{-5} for the momentum equations were used as convergence criteria.

2.3.2 Spatial and temporal discretization

The computational meshes were created using the utility `snappyHexMesh` of `foam-extend-4.0`, which generates hexahedral-dominant meshes by snapping a Cartesian mesh to the surface geometry. The final mesh is dominantly composed of hexahedral cells, i.e. the interior of the mesh consists of pure hexahedra. To fit the curved boundary, the cells near the wall are general polyhedra with a prismatic boundary-layer refinement composed of five layers. The structure of the mesh was created to provide systematically finer elements closer to the wall, instead of only the prismatic layer near the wall. Thus, a cell size grading from the interior of the mesh towards the wall was created. The mesh-independence test was performed for the vascular geometry of stage T2 using three systematically finer meshes with approximately 1.6×10^6, 4×10^6, and 7×10^6 cells. The tests were performed by comparing the hemodynamic parameters presented in Sect. 2.4 for each mesh. The results for the time-averaged wall shear stress (TAWSS) and OSI are shown in Fig. 5, while Fig. 6 shows the results for the instantaneous surface-averaged WSS, $\langle \tau_w \rangle (t)$. As can be seen in these figures, a mesh with approximately 4×10^6 control volumes can be used to obtain mesh-independent results.

Based on previous simulations performed for similar vascular geometries, a time-step of 1×10^{-5} s has been used. Three cardiac cycles were solved to avoid initial transient errors, but only the third one was analyzed in the results.

2.4 Data analysis

The instantaneous WSS vector field, $\boldsymbol{\tau}_w$, is defined on a surface S as:

$$\boldsymbol{\tau}_w(\boldsymbol{x}, t) = \boldsymbol{t} - (\boldsymbol{n} \cdot \boldsymbol{t}) \boldsymbol{n}, \qquad (7)$$

where $\boldsymbol{t}$ is the viscous traction on the surface, $\boldsymbol{t} = \boldsymbol{n} \cdot \boldsymbol{\tau}$, and $\boldsymbol{\tau}$ is the viscous part of the Cauchy stress tensor, given by Eq. (3). The peak systole wall shear stress (PSWSS) is defined as:

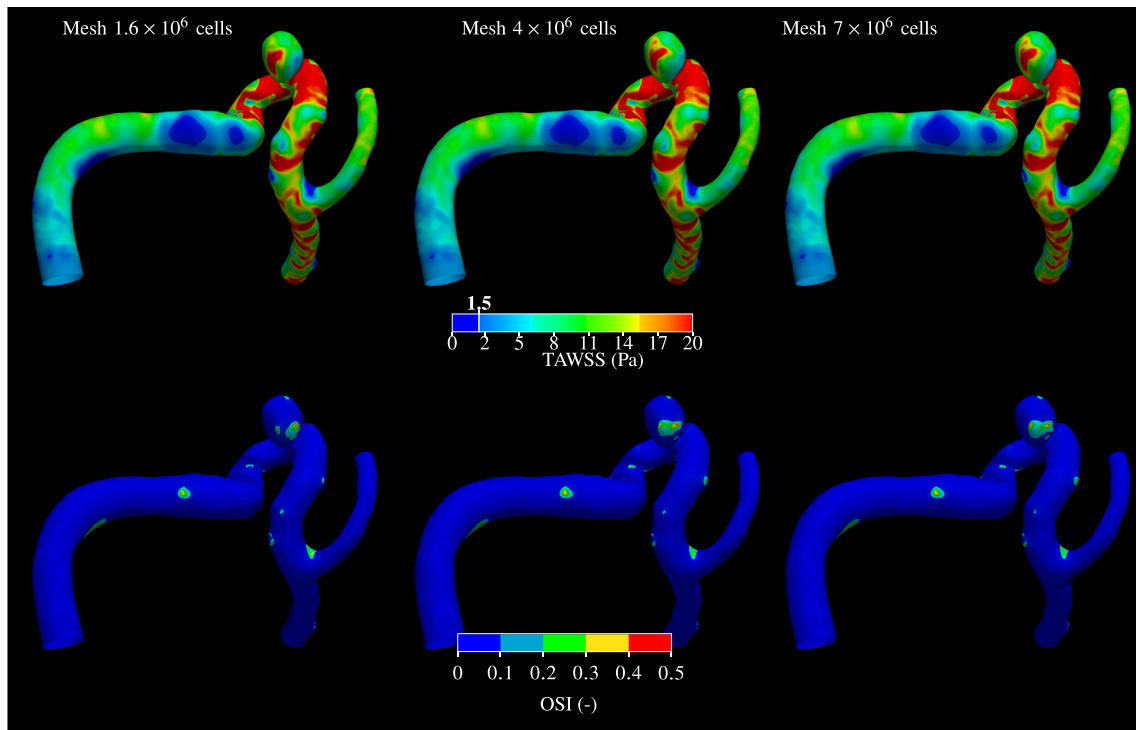$$\mathrm{PSWSS}(\boldsymbol{x}) \equiv \| \boldsymbol{\tau}_w (\boldsymbol{x}, t_{\mathrm{ps}}) \|, \qquad (8)$$

where t_{ps} is the peak systole instant—indicated by a red circle in Fig. 3.

The TAWSS field, TAWSS($\boldsymbol{x}$), and the oscillatory shear index field, OSI($\boldsymbol{x}$), defined by Eqs. (9) and (10), were also used to analyze the results:
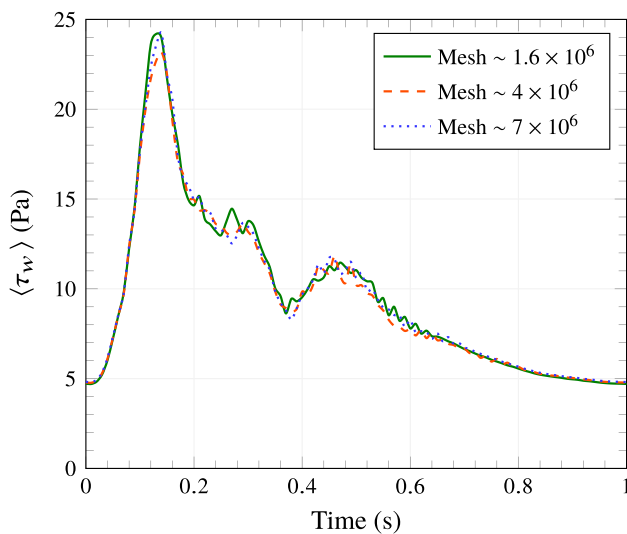
$$\mathrm{TAWSS}(\boldsymbol{x}) \equiv \overline{\tau_w}(\boldsymbol{x}) = \frac{1}{T} \int_0^T \| \boldsymbol{\tau}_w(\boldsymbol{x}, t) \| \mathrm{d}t \qquad (9)$$

and

$$\mathrm{OSI}(\boldsymbol{x}) = \frac{1}{2} \left(1 - \frac{\left\| \frac{1}{T} \int_0^T \boldsymbol{\tau}_w(\boldsymbol{x}, t) \mathrm{d}t \right\|}{\frac{1}{T} \int_0^T \| \boldsymbol{\tau}_w(\boldsymbol{x}, t) \| \mathrm{d}t} \right), \qquad (10)$$

Fig. 5 TAWSS and OSI fields on the vasculature surface at the stage T2 for computational meshes with $\sim 1.6 \times 10^6$, $\sim 4 \times 10^6$, and $\sim 7 \times 10^6$ cells

Fig. 6 Surface-averaged WSS over time for the three meshes tested on the aneurysm sac surface at stage T2

where T is the cardiac cycle period.

Two very used metrics were also computed only on the surface of the aneurysm sac, S_a, to evaluate the results. The surface-averaged WSS_{avg}, which is the average of the $TAWSS(x)$,

$$WSS_{avg} = \frac{1}{A_a} \int_{S_a} TAWSS(x) dS_a,$$ (11)

and the surface-averaged OSI, OSI_{avg}:

$$OSI_{avg} = \frac{1}{A_a} \int_{S_a} OSI(x) dS_a,$$ (12)

where A_a is the aneurysm sac surface area.

The maximum values of the TAWSS field on the aneurysm sac, S_a:

$$WSS_{max} = \max_{x \in S_a} TAWSS(x),$$ (13)

and the maximum value of the OSI field on the aneurysm sac, OSI_{max},

$$OSI_{max} = \max_{x \in S_a} OSI(x).$$ (14)

were also analyzed.

To quantify the spatial variation of the TAWSS, the time-averaged WSS gradient (TAWSSG) field, $TAWSSG(x)$, as defined by Geers et al. [12], was also computed:

$$TAWSSG(x) = \left(\nabla_t \overline{\tau_w} \right) \cdot p,$$ (15)

where ∇_t is the tangential or surface gradient operator, given by:

$$\nabla_t \equiv \nabla - \boldsymbol{n}(\boldsymbol{n} \cdot \nabla), \tag{16}$$

where ∇ is the gradient operator in Cartesian coordinates and $\boldsymbol{p}$ is the unit vector pointing in the time-averaged WSS vector direction:

$$\boldsymbol{p} = \frac{\int_0^T \boldsymbol{\tau}_w(\boldsymbol{x}, t)\mathrm{d}t}{\left\|\int_0^T \boldsymbol{\tau}_w(\boldsymbol{x}, t)\mathrm{d}t\right\|}. \tag{17}$$

The instantaneous surface-averaged WSS on the aneurysm sac surface over time, $\langle \tau_w \rangle(t)$, which provides the total tangential viscous traction on aneurysm surface, was also computed as:

$$\langle \tau_w \rangle(t) = \frac{1}{A_a} \int_{S_a} \|\boldsymbol{\tau}_w\|\mathrm{d}S_a. \tag{18}$$

Finally, the AFI, proposed originally by Mantha et al. [14], and defined as:

$$\mathrm{AFI}(\boldsymbol{x}, t) = \frac{\boldsymbol{\tau}_w(\boldsymbol{x}, t)}{\|\boldsymbol{\tau}_w\|} \cdot \boldsymbol{p} \tag{19}$$

was also analyzed.

In the Results and discussion section, high values of WSS are generally assumed higher than 10–20 Pa, whereas low WSS values usually range from 1.5 to 2.5 Pa [5]. These values were taken just as reference, as 1.5 Pa is usually associated with endothelial cell damage [39].

2.4.1 Growth analysis

To quantify the growth of the aneurysm and explore its relation with the aforementioned hemodynamic parameters, the point-wise distance between the aneurysm surfaces for consecutive stages was computed using the following procedure.

First, only the aneurysm sac portion of the vasculature at stages T1 and T2 was extracted by manually selecting the aneurysm neck contour. Since at stage T0 the aneurysm is absent, the region of the aneurysm inception on the parent artery was virtually reconstructed by comparison with the aneurysm region at stage T1 (the blue portion on the vasculature in Fig. 7a). This was accomplished after registering the vascular surface of the stage T2 to the surface of stage T1, by using the *iterative closest point* algorithm [40] implemented in VMTK®, as shown in Fig. 7b. At the end of this procedure, three surfaces were obtained: S_{T0} for stage T0, and the aneurysm surfaces for stages T1 and T2, S_{T1} and S_{T2}, respectively (shown in light gray in Fig. 7b).

Subsequently, the minimum point-wise distance between the surfaces of the two consecutive stages was computed using VMTK®, i.e. between surfaces S_{T0} and S_{T1}, and between S_{T1} and S_{T2}, respectively. These distances were interpreted as *growth distance fields* defined on the aneurysm sac surfaces, allowing to split the growth of the aneurysm into two periods: growth period 1, defined between stages T0 and T1 and characterized by the distance field d_{01}; and growth period 2, defined between stages T1 and T2 and characterized by the distance field d_{12}. Both fields d_{01} and d_{12} are, consequently, defined on the surfaces S_{T0} and S_{T1}, respectively. Correlations between these parameters and the hemodynamic parameters on the aneurysm sac surface were investigated for each growth period by considering that the points on each surface were samples subject to statistical analysis.
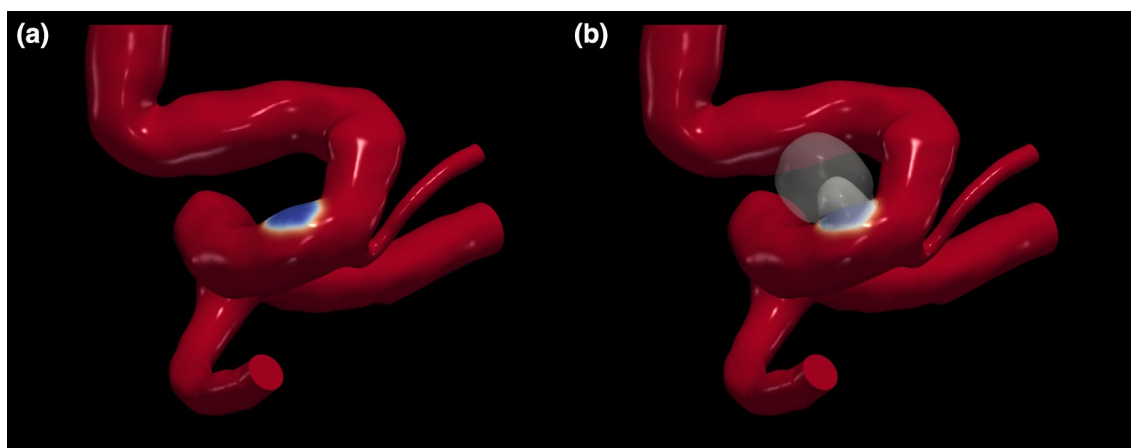
Fig. 7 Aneurysm surface selection used for the growth analysis: **a** region of the inception of the aneurysm in blue, **b** aneurysms surfaces at stages T1 and T2 in light gray, overlapped on the healthy vasculature after surface registration

3 Results and discussion

3.1 Hemodynamic analysis

Figure 8 shows the PSWSS (x) and the TAWSS (x) fields on the whole surface over one cardiac cycle for the three geometries, together with the detailed fields only on the surface of the aneurysm sac. These results show that the overall PSWSS is much higher than the reference value of 1.5 Pa on the aneurysm surface for both evolution stages. However, regions with lower levels of WSS—but still higher than 1.5 Pa—appear at stage T2 (green and blue patches of the aneurysm surface). The TAWSS field present similar patterns, but with lower values, which is an expected result because TAWSS also accounts for the WSS values along the diastole. It is important to highlight that at the initiation site of the aneurysm, PSWSS (Fig. 8a) and TAWSS (Fig. 8d) are both very high. It can also be observed that the TAWSSG (Fig. 8j) presents high positive values at the initiation site of the aneurysm. These results agree with previous researches that concluded that high levels of WSS and high positive TAWSSG are responsible for the initiation of intracranial aneurysms [12, 13]. In addition, Fig. 9 shows that the instantaneous surface-averaged WSS, $\langle \tau_w \rangle (t)$, decreases after the peak systole, evidencing the increase of low WSS area over time. This figure also shows the decrease of $\langle \tau_w \rangle (t)$ at stage T2.

The decreasing WSS levels over the aneurysm growth period can be explained by the pattern of the intra-aneurysmal flow type. As can be seen in Fig. 10a, a recirculation zone with relatively high velocities, and consequently with high WSS levels, begins to form inside the aneurysm sac at stage T1. The size of the recirculation zone increases with the growth of the aneurysm sac (Fig. 10b), inducing lower velocities at stage T2. This is a typical flow pattern that occurs in lateral aneurysms, yielding smaller velocity levels in the aneurysm lumen and, consequently, decreasing the WSS levels on its inner surface [41].

Figure 11 shows the metrics WSS_{avg}, WSS_{max}, and OSI_{avg} for each stage. For stage T0, the area of the artery portion where the aneurysm effectively developed was used for the calculations (Fig. 7a). This area is equivalent to the ostium area of the aneurysm at stage T1. It is evident that the WSS_{avg} is decreasing on the aneurysm surface because of the increase of the area of low WSS, as previously explained, mainly at stage T2. However, WSS_{max} increases during the growth period. As can be seen in Figs. 8e and f, although the area of low WSS on the aneurysm sac is larger at stage T2, a small area of very high WSS still remains.

We also analyzed the OSI field over the aneurysm surface at the stages T0, T1, and T2. Figures 8g and i show

that small portions of the aneurysm surface are under the effect of higher OSI—i.e., values close to its maximum, 0.5—in regions where the WSS vector changes its direction over time during a cardiac cycle, evidencing the disturbed flow adjacent to the aneurysm lumen. Although these areas are still very small, they contribute to the increasingly higher OSI_{avg} over the aneurysm surface, as can be seen in Fig. 11c.

3.2 Growth analysis

The focus of this section in on the possible correlation between the hemodynamic parameters and the growth distance fields, d_{01} and d_{12}. It is important to note that it is assumed that the growth distance d_{01} was caused by the hemodynamic conditions on the vascular surface S_{T0}, whereas the growth distance d_{12} was caused by the hemodynamic conditions on the vascular surface S_{T1}. Hence, in the following analysis, the growth distance d_{01} is studied against the hemodynamic parameters at the stage T0, whereas the growth distance d_{12} is studied against the hemodynamic parameters at stage T1.

Figure 12 shows the correlation between the TAWSS and the TAWSSG fields and the growth distance field d_{01}, which represents the aneurysm growth between stages T0 and T1. The only difference between Fig. 12a and b is the interchange between the abscissas and the depth variables, which are represented by different colors. In Fig. 12a, it can be observed that the points with larger aneurysm growth present high values of TAWSS (higher than 20 Pa) and high positive TAWSSG (points inside the red rectangle in Fig. 12a). This is also observed in Fig. 12b.

A linear regression line and the Pearson correlation coefficient, ρ_P, were included in Fig. 12 for each set of variables. It is clear that the linear correlation between the growth distance d_{01} and both hemodynamic parameters TAWSS and TAWSSG is very weak, as indicated by the small absolute value of the Pearson coefficient. However, it indicates a positive correlation between the variables for the first period of the aneurysm growth, i.e., the higher the TAWSS and TAWSSG the larger the growth distance.

Therefore, for the first period of the aneurysm growth, the results agree with the studies by Geers et al. [12] and Lauric et al. [13], which concluded that high TAWSS and high positive TAWSSG favor the initiation of instracranial aneurysms. It can be observed in Fig. 8 that very high TAWSS values (higher than 20 Pa) were found in the aneurysmal region at stage T0, and in Fig. 12 it is clear that the the TAWSSG field is dominantly positive for the points of larger growth.

Figure 13 shows the correlations between the TAWSS, OSI, and the growth distance field for the second period of the aneurysm growth, d_{12}. In Fig. 13a, it can be noticed that the larger values of the OSI are concentrated in the
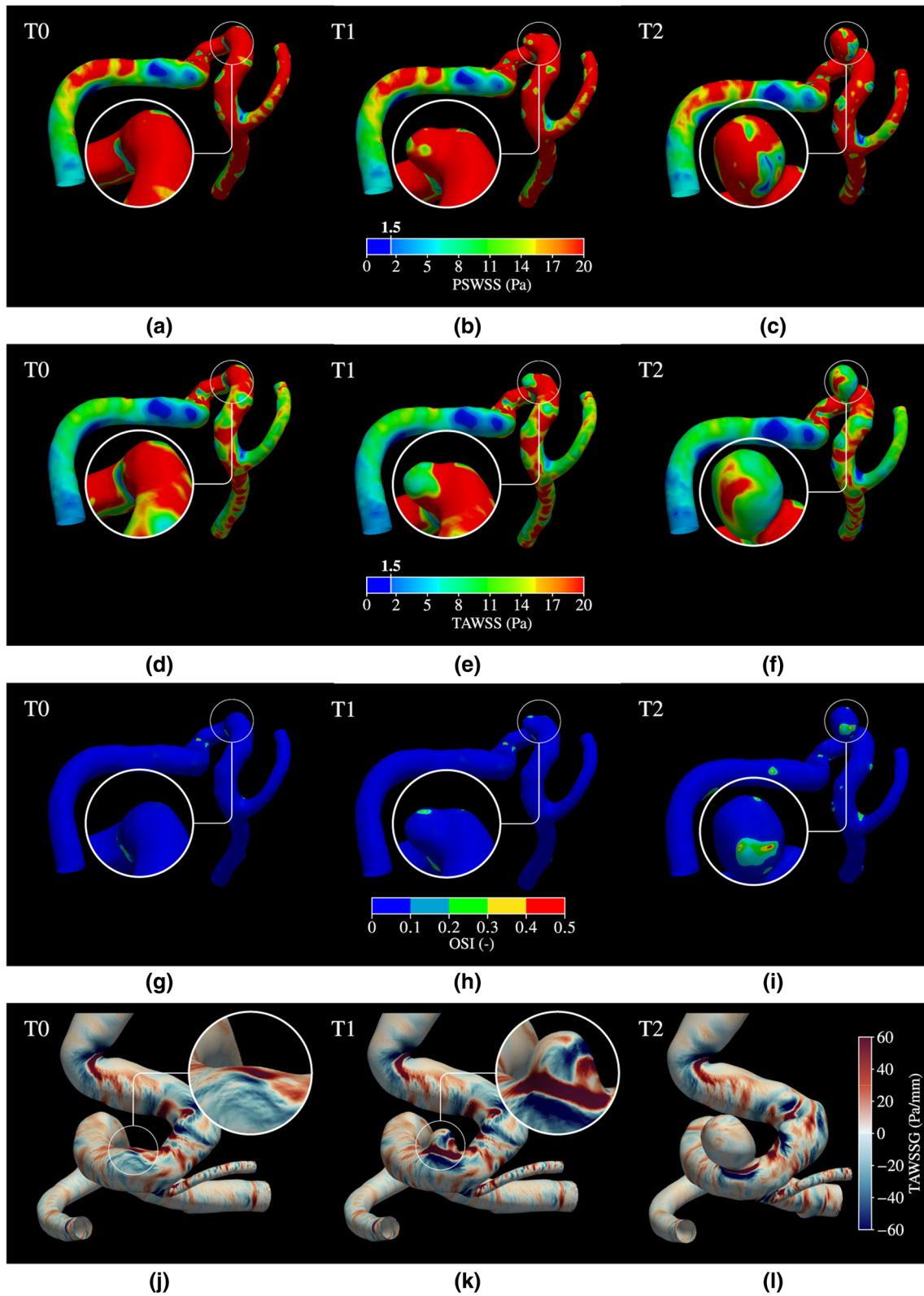
Fig. 8 Hemodynamic characterization of the WSS on the whole vascular surface and detail of the aneurysm sac surface at stages T0, T1, and T2, respectively: **a**, **b**, and **c** show the PSWSS; **d**, **e**, and **f** show the TAWSS; **g**, **h**, and **i** show the OSI; and **j**, **k**, and **l** show the TAWSSG
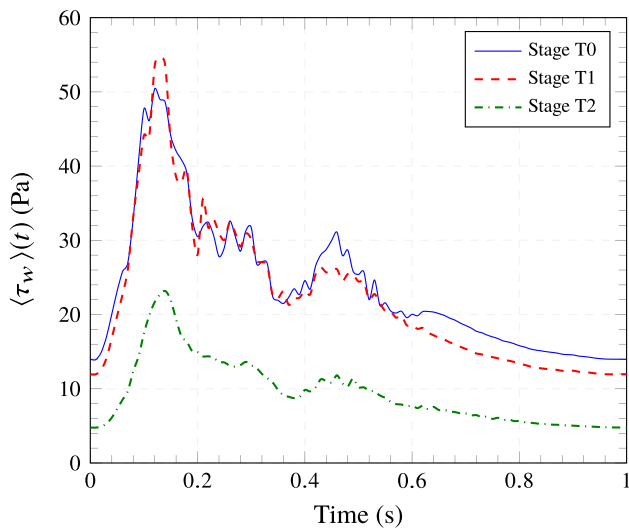
Fig. 9 Surface-averaged WSS $\langle\tau_w\rangle(t)$, over one cardiac cycle for each stage, evidencing the decrease in the WSS for the whole cardiac cycle

region of smaller TAWSS (points inside the red rectangle). This also can be observed in Fig. 13c by the kernel density estimation between the growth distance and the TAWSS, where the concentration of points is close to the blue line at TAWSS = 5 Pa. Figure 13b shows the same variables in the coordinate axes, but the depth variable is the TAWSSG. It can be noticed that the TAWSSG is predominantly zero and, therefore, seems to play no role in the second period of the aneurysm growth.

The AFI parameter was also computed. However, as in Chen et al. [42] and Geers et al. [12], a correlation between the regions of low AFI with the site of the aneurysm initiation was not found. Moreover, as shown by Geers et al. [12], OSI and AFI fields are strongly correlated, implying that these variables capture the same flow features generated on the aneurysm surface. Thus, since OSI does not seem to play a role in the aneurysm formation for the case studied here, it is understandable that the AFI yields a similar conclusion.
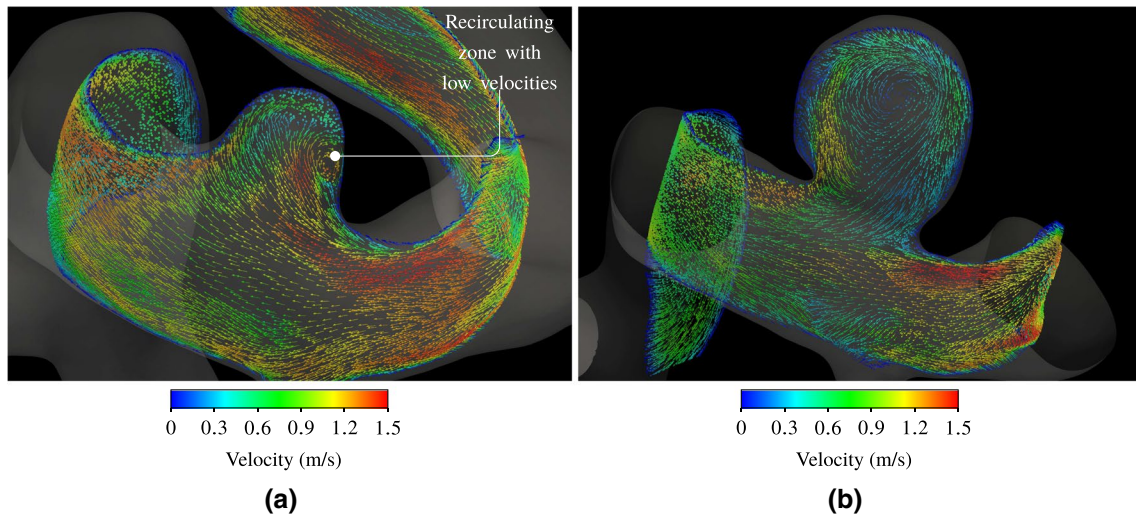
Fig. 10 Flow velocity vector field in the aneurysm **a** at stage T1 and **b** at stage T2
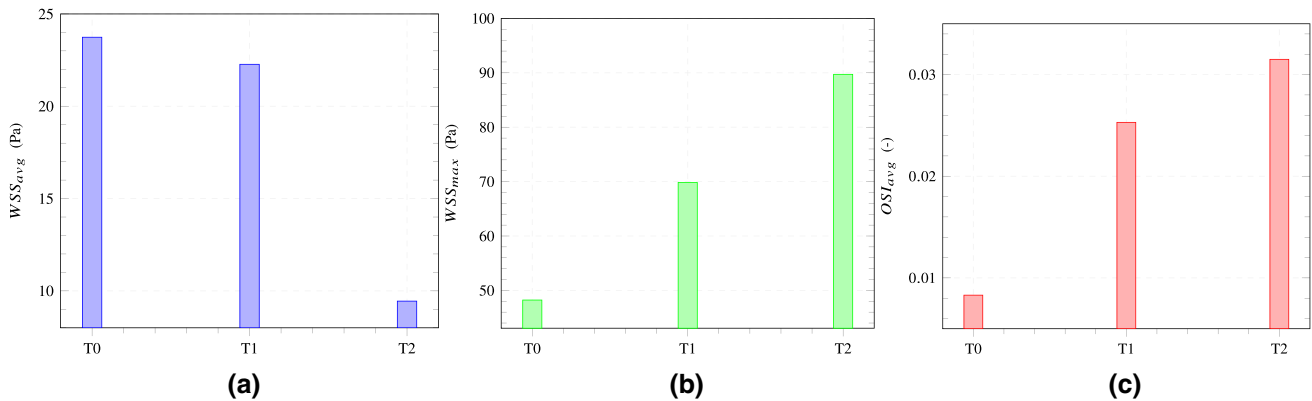
Fig. 11 WSS and OSI metrics over the aneurysm surface at each stage: **a** WSS$_{avg}$, **b** WSS_{max}, and **c** OSI$_{avg}$
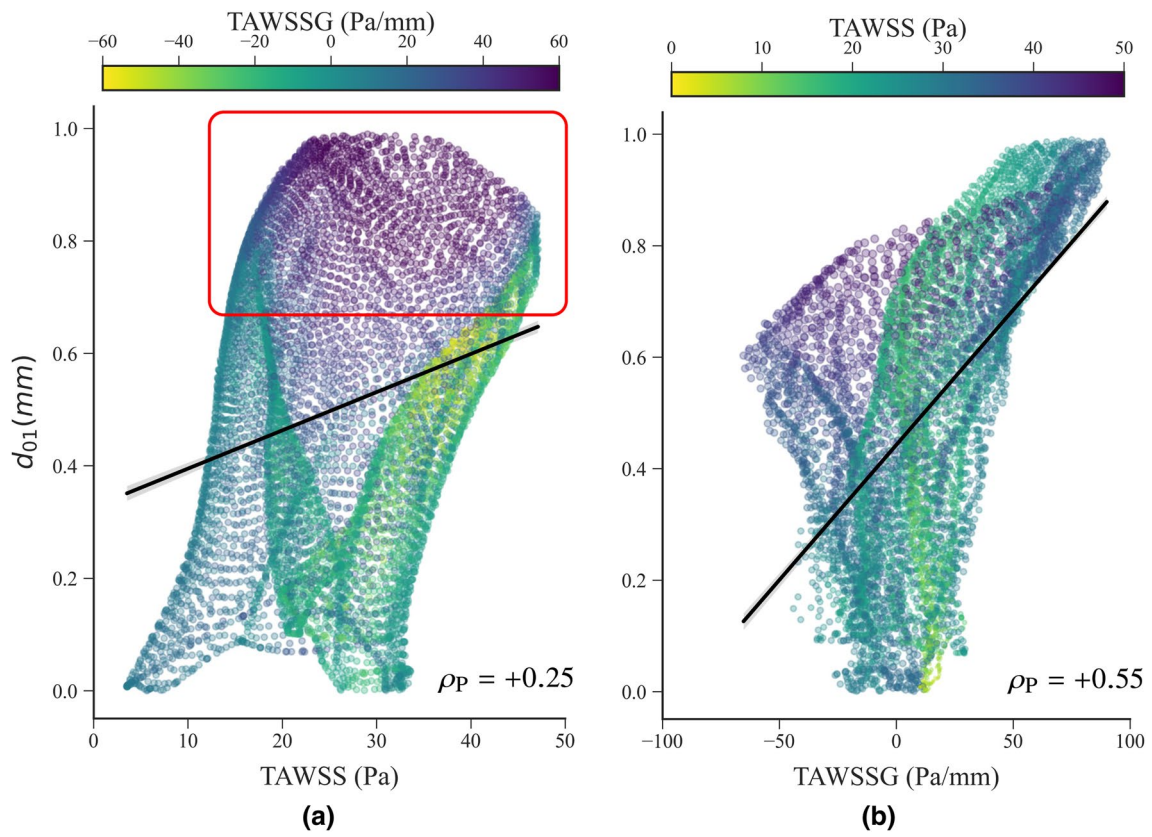
Fig. 12 Correlations between aneurysm growth distance field d_{01} and the TAWSS and TAWSSG
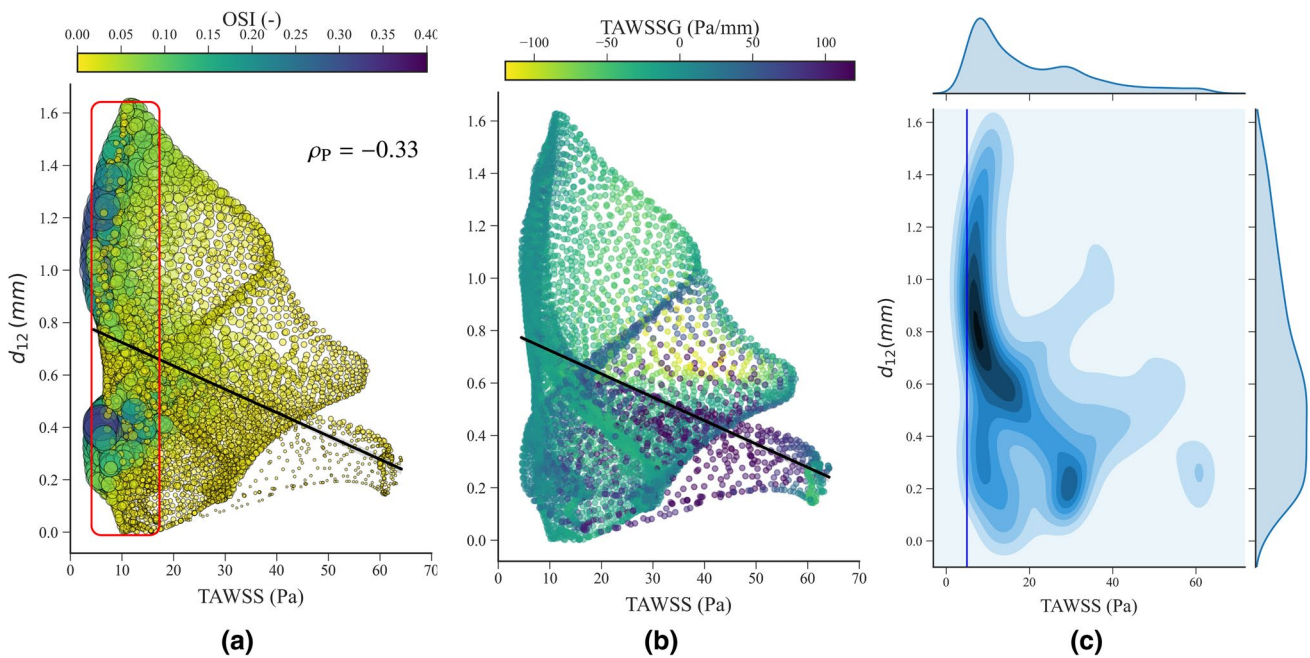

Fig. 13 Correlations between aneurysm growth distance field d_{12} and the TAWSS, TAWSSG, and OSI fields

Table 1 Three-dimensional shape indices for the aneurysm: the undulation and non-sphericity indices computed as defined by Raghavan et al. [43]

	Non-sphericity Index (–)	Undulation Index (–)
Stage T1	0.043	15.6×10^{-3}
Stage T2	0.148	5.5×10^{-3}

In summary, in the first period of the aneurysm growth, high TAWSS and high positive TAWSSG correlated positively with the aneurysm growth, which agrees with the main current theory that explain intracranial aneurysms formation. However, there is no unique theory explaining intracranial aneurysms growth, on the contrary, two major theories exist based on different hemodynamic effects. The results presented here showed that high OSI and small TAWSS values play the major role on the second period of the aneurysm. Hence, this effectively identifies the low-flow theory pathway as the driving mechanism behind the growth of this aneurysm. Furthermore, by contrasting the plots in Figs. 12 and 13, one can state that the hemodynamic data clearly reveal the change of the mechanism that drove the aneurysm growth.

If hemodynamics drives aneurysm growth, it also influences the aneurysm morphology. Table 1 shows two indices defined by Raghavan et al. [43] to evaluate the shape of an aneurysm. The non-sphericity index measures how close the aneurysm morphology is to a hemisphere—zero indicates a perfect hemisphere and one a collapsed aneurysm—whereas the undulation index quantifies the presence of blebs or lobular regions on the aneurysm surface. The low values of the non-sphericity and undulation indices computed at each growing stage reveal that the aneurysm evolved in a spherical shape, as can also be observed qualitatively in Fig. 2. These results suggest that the aneurysm growth could be due to a single mechanism influencing the whole aneurysm sac surface. Different mechanisms acting on different portions of the aneurysm surface would probably lead to blebs or lobular regions on the surface, hence, to a more irregular surface [44]. Moreover, the aneurysm growth analysis performed could help predict whether any of these morphological changes may occur on the aneurysm surface because groups of points with specific hemodynamic characteristics—shown in the format of Fig. 12 and 13—could be mapped back on to the aneurysm sac surface. Therefore, this study presents an analysis that can be used to predict how an aneurysm can grow and help identify regions prone to develop bleb and lobular regions, once the mechanisms responsible for these two morphological features are found [45].

It is worth noting that this kind of study seems to be a good example of how CFD can be a complementary tool to clinically study aneurysms cases. Nevertheless, as suggested in literature discussions [46], CFD should be included in the medical practice with warnings of its limitations, simplifications, and complexities.

4 Conclusions

This work used the CFD methodology to study longitudinally the flow dynamics in a patient-specific lateral intracranial aneurysm. The objective was to investigate the main hemodynamic parameters related to the anatomy and growth of the intracranial aneurysm, following its evolution during 5 years, and virtually reconstructing the hypothetical healthy parent artery to predict the hemodynamic pattern in the inception of the aneurysm. A complete description of the flow was provided and the main hemodynamic parameters usually accepted as playing crucial roles in this pathology were correlated with parameters quantifying the growth of the aneurysm.

The analysis of the hemodynamic parameters at each stage of the aneurysm growth was important in itself. However, when the hemodynamics parameters are combined with the data of the aneurysm growth field, the analysis becomes even more valuable. This analysis was only possible because two consecutive DSA exams of the same aneurysm were available. The results revealed that the aneurysm probably initiated mainly due to high levels of WSS and high positive values of TAWSSG. This conclusion agrees with the most accepted hypothesis on intracranial aneurysm formation. The results also suggest that the subsequent growth of the aneurysm was due to the combination of low WSS and high OSI values. Hence, to the authors' knowledge, this might be the first study identifying the mechanism behind the aneurysm growth in a scenario where two mainstream theories explain intracranial aneurysms growth over time. For clinicians, this can be a valuable information as it can potentially help identify the regions prone to dangerous manifestations of growth, such as blebs, normally associated with sites of aneurysm rupture.

References

1. Nieuwkamp DJ, Setz LE, Algra A, Linn FHH, de Rooij NK, Rinkel GJE (2009) Changes in case fatality of aneurysmal subarachnoid haemorrhage over time, according to age, sex, and

region: a meta-analysis. Lancet Neurol 8:635–642. https://doi.org/10.1016/S1474, http://www.thelancet.com/neurology

2. van Gijn J, Rinkel GJE, Gijn JV, Rinkel GJE (2001) Subarachnoid haemorrhage: diagnosis, causes and management. Brain: J Neurol 124(Pt 2):249–78. https://doi.org/10.1093/brain/124.2.249, http://www.ncbi.nlm.nih.gov/pubmed/11157554

3. Stehbens WE (1989) Etiology of intracranial berry aneurysms. J Neurosurg 70:823–831. https://doi.org/10.3171/jns.1989.70.6.0823

4. Buchanan JR, Kleinstreuer C, Truskey GA, Lei M (1999) Relation between non-uniform hemodynamics and sites of altered permeability and lesion growth at the rabbit aorto-celiac junction. Technical report

5. Malek AM, Alper SL, Izumo S (1999) Hemodynamic shear stress and its role in atherosclerosis. J Am Med Assoc 282(December):2035–2042

6. Ku DN, Giddens DP, Zarins CK, Glagov S (1985) Pulsatile flow and atherosclerosis in the human carotid bifurcation. Positive correlation between plaque location and low oscillating shear stress. Arteriosclerosis 5(3):293–302, http://www.ncbi.nlm.nih.gov/pubmed/3994585

7. Dolan JM, Kolega J, Meng H (2013) High wall shear stress and spatial gradients in vascular pathology: a review. Ann Biomed Eng 41(July):1411–1427. https://doi.org/10.1007/s10439-012-0695-0

8. Meng H, Wang Z, Hoi Y, Gao L, Metaxa E, Swartz DD, Kolega J, Swartz DD, Kolega J (2007) Complex hemodynamics at the apex of an arterial bifurcation induces vascular remodeling resembling cerebral aneurysm initiation. Stroke 38:1924–1931. https://doi.org/10.1161/STROKEAHA.106.481234

9. Soldozy S, Norat P, Elsarrag M, Chatrath A, Costello JS, Sokolowski JD, Tvrdik P, Kalani MYS, Park MS (2019) The biophysical role of hemodynamics in the pathogenesis of cerebral aneurysm formation and rupture. Neurosurg Focus 47(1):1–9. https://doi.org/10.3171/2019.4.focus19232

10. Metaxa E, Tremmel M, Natarajan SK, Xiang J, Paluch RA, Mandelbaum M, Siddiqui AH, Kolega J, Mocco J, Meng H (2010) Characterization of critical hemodynamics contributing to aneurysmal remodeling at the basilar terminus in a rabbit model. Stroke 41(8):1774–1782. https://doi.org/10.1161/STROKEAHA.110.585992

11. Meng H, Tutino VM, Xiang J, Siddiqui A (2014) High WSS or Low WSS? complex interactions of hemodynamics with intracranial aneurysm initiation, growth, and rupture: toward a unifying hypothesis. Am J Neuroradiol 35(7):1254–1262. https://doi.org/10.3174/ajnr.A3558

12. Geers AJ, Morales HG, Larrabide I, Butakoff C, Bijlenga P, Frangi AF (2017) Wall shear stress at the initiation site of cerebral aneurysms. Biomech Model Mechanobiol 16:97–115. https://doi.org/10.1007/s10237-016-0804-3

13. Lauric A, Hippelheuser J, Safain MG, Malek AM (2014) Curvature effect on hemodynamic conditions at the inner bend of the carotid siphon and its relation to aneurysm formation. J Biomech 47(12):3018–3027. https://doi.org/10.1016/j.jbiomech.2014.06.042

14. Mantha A, Karmonik C, Benndorf G, Strother C, Metcalfe R (2006) Hemodynamics in a cerebral artery before and after the formation of an aneurysm. Am J Neuroradiol 27:1113–1118, www.ajnr.org

15. Shimogonya Y, Ishikawa T, Imai Y, Matsuki N, Yamaguchi T (2009) Can temporal fluctuation in spatial wall shear stress gradient initiate a cerebral aneurysm? a proposed novel hemodynamic index, the gradient oscillatory number (GON). J Biomech 42:550–554

16. He X, Ku DN, Engineering B, He X (2016) Researcher I (1996) pulsatile flow in the human left coronary artery bifurcation: average conditions. J Biomech Eng 118:74–82. https://doi.org/10.1115/1.2795948

17. Sforza DM, Putman CM, Cebral JR (2009) Hemodynamics of cerebral aneurysms. Ann Rev Fluid Mech 41(1):91–107. https://doi.org/10.1146/annurev.fluid.40.111406.102126, http://www.annualreviews.org

18. Ma B, Harbaugh RE, Raghavan ML (2004) Three-dimensional geometrical characterization of cerebral aneurysms. Ann Biomed Eng 32(2):264–273

19. Dhar S, Tremmel M, Mocco J, Kim M, Yamamoto J, Siddiqui AH, Hopkins LN, Meng H (2008) Morphology parameters for intracranial aneurysm rupture risk assessment. Neurosurgery 63(2):185–196. https://doi.org/10.1227/01.NEU.0000316847.64140.81

20. Xiang J, Natarajan SK, Tremmel M, Ma D, Mocco J, Hopkins LN, Siddiqui AH, Levy EI, Meng H (2011) Hemodynamic-morphologic discriminants for intracranial aneurysm rupture. Stroke 42(1):144–152. https://doi.org/10.1161/STROKEAHA.110.592923

21. Cebral JR, Mut F, Weir J, Putman CM (2011a) Association of hemodynamic characteristics and cerebral aneurysm rupture. Am J Neuroradiol 32:264–270. https://doi.org/10.3174/ajnr.A2274

22. Cebral JR, Mut F, Weir J, Putman C (2011b) Quantitative characterization of the hemodynamic environment in ruptured and unruptured brain aneurysms. Am J Neuroradiol 32:145–151. https://doi.org/10.3174/ajnr.A2419

23. Boussel L, Rayz V, Mcculloch C, Martin A, Acevedo-Bolton G, Lawton M, Higashida R, Smith WS, Young WL, Saloner D (2008) Aneurysm growth occurs at region of low wall shear stress: patient-specific correlation of hemodynamics and growth in a longitudinal study. Stroke 39:2997–3002. https://doi.org/10.1161/STROKEAHA.108.521617, http://stroke.ahajournals.org

24. Sforza DM, Putman C, Tateshima S, Viñuela F, Cebral J (2011) Time evolution and hemodynamics of cerebral aneurysms. In: Proceedings of SPIE, https://doi.org/10.1117/12.877703

25. Piccinelli M, Veneziani A, Steinman DA, Remuzzi A, Antiga L (2009) A framework for geometric analysis of vascular structures: application to cerebral aneurysms. IEEE Trans Med Imaging 28(8):1141–1155. https://doi.org/10.1109/TMI.2009.2021652

26. Chnafa XC, Brina XO, Pereira VM, Steinman XDA (2018) Better than nothing: a rational approach for minimizing the impact of outflow strategy on cerebrovascular simulations. Am J Neuroradiol 39:337–343. https://doi.org/10.3174/ajnr.A5484

27. Isaksen JG, Bazilevs Y, Kvamsdal T, Zhang Y, Kaspersen JH, Waterloo K, Romner B, Ingebrigtsen T (2008) Determination of wall tension in cerebral artery aneurysms by numerical simulation. Stroke 39(12):3172–3178. https://doi.org/10.1161/STROKEAHA.107.503698

28. Shibeshi SS, Collins WE (2005) The rheology of blood flow in a branched arterial system with three-dimensional model: a numerical study. Appl Rheol 15(6):398–405. https://doi.org/10.1017/S1727719100002951

29. Fung YC (1993) Biomechanics: motion, flow, stress, and growth. Springer. https://doi.org/10.1115/1.2900838

30. Ford MD, Alperin N, Lee SH, Holdsworth DW, Steinman DA (2005) Characterization of volumetric flow rate waveforms in the normal internal carotid and vertebral arteries. Physiol Meas 26(4):477–488. https://doi.org/10.1088/0967-3334/26/4/013

31. Zarrinkoob L, Ambarki K, Wåhlin A, Birgander R, Eklund A, Malm J (2015) Blood flow distribution in cerebral arteries. J Cereb Blood Flow Metab 35:648–654. https://doi.org/10.1038/jcbfm.2014.241

32. Torii R, Oshima M, Kobayashi T, Takagi K, Tezduyar TE (2007) Influence of wall elasticity in patient-specific hemodynamic simulations. Comput Fluids 36:160–168. https://doi.org/10.1016/j.compfluid.2005.07.014

33. Torii R, Oshima M, Kobayashi T, Takagi K, Tezduyar TE (2010) Influence of wall thickness on fluid-structure interaction computations of cerebral aneurysms. Int J Numer Methods Biomed Eng 26:336–347. https://doi.org/10.1002/cnm.1289

34. foam-extend Project (2017) foam-extend Website. https://sourceforge.net/projects/foam-extend/. Accessed 19 June 2017

35. Weller HG, Tabor G, Jasak H, Fureby C (1998) A tensorial approach to computational continuum mechanics using object-oriented techniques. Comput Phys 12:620–631

36. Jasak H (1996) Error analysis and estimation for the finite volume method with applications to fluid flows. Ph.D. thesis, Imperial College

37. Moukalled F, Mangani L, Darwish M (2016) The finite volume method in computational fluid dynamics, vol 113. Springer. https://doi.org/10.1007/978-3-319-16874-6

38. Issa RI (1986) Solution of the implicitly discretised fluid flow equations by operator-splitting. J Comput Phys 62(1):40–65. https://doi.org/10.1016/0021-9991(86)90099-9

39. Shojima M, Oshima M, Takagi K, Torii R, Hayakawa M, Katada K, Morita A, Kirino T (2004) Magnitude and role of wall shear stress on cerebral aneurysm. Computational fluid dynamic study of 20 middle cerebral artery aneurysms. Stroke 35(11):2500–2505. https://doi.org/10.1161/01.STR.0000144648.89172.of

40. Besl PJ, McKay ND (1992) A method for registration of 3-D shapes. IEEE Trans Pattern Anal Mach Intell 14:239–256

41. Le TB, Borazjani I, Sotiropoulos F (2010) Pulsatile flow effects on the hemodynamics of intracranial aneurysms. J Biomech Eng 132:1–11. https://doi.org/10.1115/1.4002702

42. Chen H, Selimovic A, Thompson H, Chiarini A, Penrose J, Ventikos Y, Watton PN (2013) Investigating the influence of haemodynamic stimuli on intracranial aneurysm inception. Ann Biomed Eng 41(July):1492–1504. https://doi.org/10.1007/s10439-013-0794-6

43. Raghavan ML, Ma B, Harbaugh RE (2005) Quantified aneurysm shape and rupture risk. J Neurosurg 102(2):355–362. https://doi.org/10.3171/jns.2005.102.2.0355

44. Tateshima S, Murayama Y, Villablanca JP, Morino T, Nomura K, Tanishita K, Viñuela F (2003) In vitro measurement of fluid-induced wall shear stress in unruptured cerebral aneurysms harboring blebs. Stroke 34(1):187–192. https://doi.org/10.1161/01.STR.0000046456.26587.8B

45. Salimi Ashkezari SF, Mut F, Chung BJ, Robertson AM, Cebral JR (2020) Hemodynamic conditions that favor bleb formation in cerebral aneurysms. J NeuroInterv Surg. https://doi.org/10.1136/neurintsurg-2020-016369

46. Cebral JR, Meng H (2012) Counterpoint: realizing the clinical utility of computational fluid dynamics: closing the gap. https://doi.org/10.3174/ajnr.a2993